Schwank, M., Stähli, M., Wydler, H., Leuenberger, J., Mätzler, C., Flühler, H. (2004): Microwave L-Band Emission of Freezing Soil. - IEEE Transactions on Geoscience and Remote Sensing, 42, 6, 1252-1261

DOI: 10.1109/TGRS.2004.825592

Microwave L-Band Emission of Freezing Soil

Mike Schwank, Manfred Stähli, Hannes Wydler, Joerg Leuenberger, Christian Mätzler, *Senior Member, IEEE*, and H. Flühler

***Abstract*—We report on field-measured microwave emission in a period of frost penetration into a grassland soil. The measurements were recorded with a high temporal resolution using an L-band radiometer mounted on a 7-m high tower. The observation period (December 2002 to March 2003) included two cycles of soil freezing and thawing with maximum frost depth of 25 cm. *In situ* soil temperature and liquid water content were measured at five depths down to 45 cm. Soil moisture profiles were calculated using the COUP numerical soil water and heat model in combination with measured soil properties and meteorological data monitored at the site. The L-band radiation data clearly showed the penetration and thawing of seasonal soil frost. We calculated soil reflectivities based on *in situ* measured and modeled soil moisture profiles by applying a coherent radiative transfer model. The calculated reflectivities were compared with the radiometrically determined soil reflectivities. It was demonstrated that the quantitative consistency between these reflectivities was significantly improved by applying an impedance matching approach accounting for surface effects. In this particular case, the dielectric structure of the uppermost soil horizon was largely influenced by soil roughness, vegetation, and snow cover. The radiometrically measured soil reflectivities were fitted using a radiative transfer model in combination with a roughness model assuming a soil surface roughness of 25 mm. The analysis during a period of frost penetration shows coherent behavior of the soil reflectivity. Temporal oscillation of the measured L-band radiation appears to be a coherent effect. This effect has the potential to be used for estimating the frost penetration velocity.**

***Index Terms*—Dielectric measurements, frozen soil, ice, microwave radiometry, remote sensing, soil measurements, soil water content.**

I. Introduction

MORE THAN one third of the earth's land surface is subject to seasonal or permanent soil frost. This has a significant impact on many agricultural, engineering, and environmental issues and applications. A frozen land surface tends to reduce or—in the worst case—impede water infiltration, which may promote water ponding on fields, surface runoff, and soil erosion [1]. Frost-induced soil heaving poses a problem to constructors of roads, railroads, pipelines, and buildings. Land surface heat exchange is strongly influenced by the presence of frozen soil and needs, therefore, to be considered in meteorological models [2]. Also, the root water uptake in boreal forests [3] or the stability of slopes [4] may be affected by frozen soil. For these reasons, there is a great demand for techniques to monitor the spatial and temporal extent of soil frost as well as its characteristics (e.g., frost depth). In the field of remote sensing, some studies have been presented on soil frost detection and mapping. Since a frozen soil is (hydrologically speaking) similar to a very dry soil, it appears that remote sensing methods for determining liquid water content are likely to be useful for detecting soil frost. One of the most promising approaches for measuring the large-scale soil moisture distribution is passive microwave remote sensing [5], particularly when observed at the L-band (1.4 GHz). At this low frequency of the microwave range, the measurements are not influenced by weather conditions, and the penetration depth of the radiation is quite deep [6]. Microwave emission has already been used to map soil frost (albeit very qualitatively) at the continental scale [7] using Special Sensor Microwave/Imager (SSM/I) data. The potential of microwave emission remote sensing to detect frozen ground was demonstrated, but also the urgent need for an improved quantitative understanding of microwave emission from frozen soils in relation to, for example frost depth and ice/liquid water contents, overlaying snow cover, or vegetation and roughness effects.

L-band microwave emission of soil under irrigation was investigated by Schmugge and Jackson [8]. They observed an oscillatory behavior in time, which was attributed to interferences between reflections from the air–soil interface and the wet soil–dry soil interface as the latter moved down in the soil.

This paper contributes to a better quantitative understanding of the L-band microwave emission of agricultural grassland soil as measured during one winter season including two major frost events. For this purpose, we used the newly developed ETH L-band radiometer (ELBARA) [9] mounted on a 7-m tower facing aslant to the soil surface. This instrument was originally built to measure the near-surface moisture content and was extensively used on arable land in spring and summer [10]. In these experiments, different models for interpreting the microwave signal in terms of water content were investigated.

In this paper, we present for the first time high temporal resolution radiometric L-band data showing the penetration and thawing of seasonal soil frost. The radiometer data were compared with *in situ* soil moisture profile measurements of liquid water and temperature.

The objectives of this work are as follows:

- to demonstrate the sensitivity of microwave emission to the presence of soil frost;
- to investigate the possibility to determine the soil frost penetration velocity from coherent effects affecting the measured brightness temperature;
- to identify major influences and limits for the use of L-band microwave emission for monitoring frozen ground.

Manuscript received October 14, 2003; revised January 20, 2004.

M. Schwank, H. Wydler, J. Leuenberger and H. Flühler are with the Institute of Terrestrial Ecology, ETH Zürich, 8952 Schlieren, Switzerland.

M. Stähli is with the Swiss Federal Institute for Forest, Snow and Landscape Research, 8903 Birmensdorf, Switzerland.

C. Mätzler is with the Institute of Applied Physics, University of Bern, 3012 Bern, Switzerland.

Digital Object Identifier 10.1109/TGRS.2004.825592

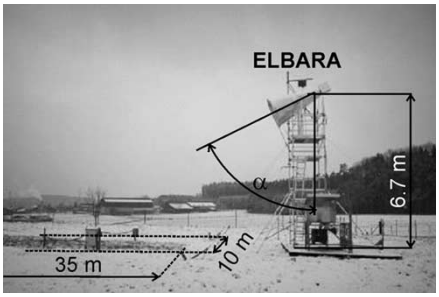

Fig. 1. L-band radiometer ELBARA on the tower at the test site.

TABLE I
SOIL PROPERTIES OF THE EXPERIMENTAL FIELD AT ESCHIKON [11] (z = soil depth [m], S = sand content [kg · kg^{-1}], C = clay content [kg · kg^{-1}], OL = organic matter [kg · kg^{-1}], θ_0 = saturated water content [m^3 · m^{-3}], K_s = saturated hydraulic conductivity [cm · h^{-1}])

z	S	C	OL	θ_0	K_s
0 – 0.15	0.413	0.267	0.057	0.45	0.322
0.15 – 0.45	0.343	0.300	0.016	0.42	1.058
> 0.45	0.318	0.279	0.002	0.36	0.0094

II. FIELD EXPERIMENT

A. Field Site and Measurements

The field experiment was set up to study soil freezing and thawing cycles with an L-band radiometer. The measurements were carried out on a flat grass-covered field at the Institute of Plant Sciences, Eschikon (550 m a.s.l.), 15 km northeast of Zurich (Fig. 1). At this location, the mean January temperature is −0.6 °C, and an average winter has 34.6 days of snowfall (period 1971–2003). During the experiment, the field was covered with filiform grass up to 5 cm long. The soil was classified as a loam according to the U.S. Department of Agriculture classification scheme, consisting of rather compacted subsoil covered by an organic-rich top soil layer of approximately 20 cm. The hydraulic properties of the uppermost 60 cm were determined by inverse modeling of a drainage experiment [11] and are summarized in Table I.

To sense the emitted electromagnetic radiation of the soil, the L-band radiometer ELBARA [12] was mounted on a 6.7-m high tower. The observation angle (relative to the vertical direction) was $\alpha = 70°$ (this shallow observation angle is the consequence of a mistake during the installation of the antenna; an angle of 55° was intended), and the geographical orientation was southeast (toward sunrise).

The half axes of the elliptic surface area (footprint) sensed by the radiometer were estimated to be approximately 10 m × 35 m corresponding to the 3-dB beamwidth of the radiometer antenna. At the left and right border of this footprint, we installed thermistors (Campbell S-TL107) and two-rod TDR probes (self-constructed with Campbell TDR electronics) at eight different soil depths (20, 40, 60, 80, 100, 150, 250, and 450 mm) for recording soil temperature and liquid soil water content every 10 min.

Also, some basic meteorological variables were monitored at the site: air temperature, relative humidity, precipitation, and downwelling solar radiation. As input to the numerical model (Section III-A), we used additional weather data from Zurich Airport (provided by the national weather service MeteoSwiss), 10 km west of the test site. The snow depth on the plot was measured manually after snowfall events or significant snowmelt. However, for most of the studied period, we tried to keep the plot free of snow in order to promote soil frost development and to minimize the influence of the snow cover on the L-band measurements.

B. Remote Sensing System

We used ELBARA, operating at L-band (1.4 GHz), for microwave remote sensing measurements of the soil surface. A detailed description of ELBARA is given in [9]. ELBARA is equipped with a dual-polarized conical horn antenna with 3-dB beamwidth of 12° and symmetrical and identical beams with small sidelobes. ELBARA is a Dicke-type radiometer with an internal hot and cold load at the temperatures $T_{\rm hot}$ and $T_{\rm cold}$. When the internal hot and cold loads are measured for calibration purposes, $u_{\rm hot}$ and $u_{\rm cold}$ are the corresponding voltages, $T_{\rm Dicke}$ is the Dicke-temperature, and $U^{(p)}$ denotes the output voltage when the radiometer antenna is measuring the scene of interest (p = vertical or horizontal polarization). The brightness temperature $T_{\rm B}^{(p)}$ of the scene measured at polarization p follows from the following system-specific calibration relation:

$$T_{\rm B}^{(p)} = A \cdot U^{(p)} + T_{\rm Dicke} \text{ with } A = \frac{T_{\rm hot} - T_{\rm cold}}{u_{\rm hot} - u_{\rm cold}}. \quad (1)$$

For the experiment presented in this paper, the calibration was performed before each measurement with $T_{\rm cold} = 278$ K, $T_{\rm hot} = 338$ K, and $T_{\rm Dicke} = 315$ K. The time resolution of the radiometric measurements was 30 min for the whole observation period. Due to the flat observation angle of $\alpha = 70°$, the soil reflectivity for vertical polarization is almost insensitive to changes in the dielectric properties of the soil. Therefore, only the horizontally polarized radiation was analyzed in this work. To filter man-made electromagnetic noise, ELBARA is simultaneously working at two separated channels: between 1400–1418 MHz and 1409–1427 MHz.

III. THEORY

A. COUP Model

The numerical soil–vegetation–atmosphere transfer model COUP [13] was used to simulate soil water content profiles as input to the soil reflectivity model (Section III-C). The model is specifically designed to calculate physical processes in soils exposed to cold climates. It has been used to study snowmelt infiltration into frozen arable fields [14], runoff from a partly frozen alpine slope [15], and the thermal impact of a shallow snowpack on soil frost penetration [16]. The model calculates the vertical water and heat fluxes between soil layers based on the Richards' equation [17] and Fick's law. The hydraulic properties are parameterized based on the soil water retention curves [18]. The upper thermal boundary condition is given by the surface energy balance (optionally also accounting for vegetation and the temporal occurrence of a snowpack),

whereas at the lower boundary of the simulated soil profile, a cosine-shaped annual temperature variation is assumed. In the case of the Eschikon site, a fluctuating groundwater table defines the lower boundary condition for water flow, whereas measured precipitation, calculated evapotranspiration, and snowmelt are the water fluxes at the soil surface.

When soil freezes, the heat and water fluxes are coupled according to the general heat flow equation: for a given soil layer of thickness z, all changes in total heat storage during a time period t are balanced by the change in latent heat caused by freezing/thawing and the heat losses and inputs (q_{h}) to and from the adjacent soil layers

$$\frac{\partial(CT)}{\partial t} = L_{\mathrm{f}}\rho_{\mathrm{soil}}\frac{\partial\theta_{\mathrm{ice}}}{\partial t} + \frac{\partial}{\partial z}(-q_{\mathrm{h}}) \tag{2}$$

where C is the heat capacity, T is the soil temperature, L_{f} is the latent heat of freezing (3.338 10^5 J $\cdot$ kg^{-1}), ρ_{soil} is the soil bulk density, and θ_{ice} is the volumetric ice content.

When the soil temperature drops below 0 °C, the liquid soil water gradually transforms to ice, except for residual water content θ_{res}, which remains unfrozen even at very low temperatures

$$\theta_{\mathrm{res}} = d_1\theta_{\mathrm{wilt}} \tag{3}$$

where d_1 is an empirical parameter and θ_{wilt} is the water content at the permanent wilting point (metric potential $h = -1.5$ MPa). Phase change is assumed to take place in a temperature interval between 0 °C and a threshold temperature T_{f} (typically -5 °C). In this interval, soil temperature and gravimetric ice content w_{ice} are given by partitioning the total heat content Q into sensible heat TC and latent heat $-L_{\mathrm{f}}w_{\mathrm{ice}}$

$$Q = TC - L_{\mathrm{f}}w_{\mathrm{ice}} \tag{4}$$

according to the following empirical equation:

$$TC = Q\left(1 - \frac{L_{\mathrm{f}}w_{\mathrm{ice,f}}}{Q_{\mathrm{f}}}\right)(1 - r_{\mathrm{f}}) \tag{5}$$

where Q_{f} and $-L_{\mathrm{f}}w_{\mathrm{ice,f}}$ are the total and latent heat content at temperature T_{f}, and r_{f} is the freezing-point depression factor expressed as

$$r_{\mathrm{f}} = \left(1 - \frac{Q}{Q_{\mathrm{f}}}\right)^{d_2} \tag{6}$$

with the empirical parameter d_2.

The model is driven by daily or hourly values of five meteorological parameters: air temperature, relative humidity, wind speed, precipitation, and global radiation. The partial differential equations for water and heat are solved with an explicit forward difference method (Euler integration). A detailed description of all model parts can be found in [19].

B. Microwave L-Band Radiometry

Microwave remote sensing makes use of electromagnetic energy that is reflected and emitted by the earth's surface [20]. The L-band radiometer is sensitive in a narrow spectral range around the frequency of 1.4 GHz (corresponding to the wavelength of 21 cm). At L-band, the main contribution of the electromagnetic radiance is given by the thermal self-emission of the observed land surface. The radiance is determined by the thermodynamic temperature T_{A} and is proportional to the emissivity e of the observed area. In general, the temperature dependence of the radiance is described by Planck's Law, but at microwave frequencies, the linear Rayleigh–Jeans approximation holds. As a result of this linear relation, the radiance is identified with the so-called brightness temperature T_{B}

$$T_{\mathrm{B}} = eT_{\mathrm{A}}. \tag{7}$$

Assuming that the observed scene is in a thermodynamic equilibrium, the emissivity e is related to the reflectivity r by Kirchhoff's law

$$r = 1 - e. \tag{8}$$

As will be discussed later, the soil reflectivity r is used to compare the radiometric measurements with *in situ* measurements and simulated soil profiles (see Sections III-C and IV-B).

The soil reflectivity (and thus T_{B}) is a strong function of the liquid free-soil-water content due to the large contrast between the dielectric constant of free water ($\varepsilon_{\mathrm{w}} \approx 80$) and dry soil ($\varepsilon_{\mathrm{matrix}} \approx 3$ to 5) at 1.4 GHz. This allows us to derive the soil moisture from the soil reflectivity r by applying dielectric mixing and radiative transfer models. In the simplest case, the radiative transfer model is represented by the Fresnel equations, which express the soil reflectivity r as a function of the dielectric constant [20], assumed to be uniform within the soil. This model is often used for the determination of the soil moisture from radiometric data [21]. However, the water content derived in this way is in many cases not comparable to the values obtained from other soil moisture detection techniques such as time-domain reflectometry (TDR) [22]. For this reason, soil reflectivities were compared among each other instead of soil moisture values. The compared soil reflectivities were either based on radiometric observations or on soil moisture profiles derived from *in situ* measurements or simulations. The soil temperature T_{A} in (7) was calculated as an effective soil temperature causing a given emission [23]

$$T_{\mathrm{A}} = \frac{1}{\cos(\alpha)}\int_0^\infty T(z)\gamma_{\mathrm{a}}(z)e^{-\tau(z)/\cos(\alpha)}dz$$

with

$$\tau(z) = \int_0^z \gamma_{\mathrm{a}}(z')dz'. \tag{9}$$

In this equation, the T_{A} is obtained from the soil temperature profile $T(z)$ within the top 20–40 cm (depending on the water content). Thereby, the decreasing influence of deeper soil layers is considered by the absorption coefficient $\gamma_{\mathrm{a}}(z)$ from which the opacity $\tau(z)$ from depth z to the soil surface at $z = 0$ is calculated. The absorption coefficient $\gamma_{\mathrm{a}}(z)$ is related to the real and imaginary part of the dielectric constant $\varepsilon(z) = \varepsilon'(z) - \mathrm{j}\cdot\varepsilon''(z)$ at depth z

$$\gamma_{\mathrm{a}}(z) \cong \frac{2\pi}{\lambda}\frac{\varepsilon''(z)}{\sqrt{\varepsilon'(z)}} \text{ for } \varepsilon'' < \varepsilon'. \tag{10}$$

C. Calculation of Soil Reflectivity

In this paper, soil reflectivity is the crucial quantity used to compare radiometric data with TDR- and modeled soil data. Therefore, we calculated three different reflectivities: 1) r_{TDR} based on the *in situ* measured TDR and temperature data; 2) r_{COUP} based on soil water content profiles simulated with a numerical soil water and heat model (COUP; see Section III-A); and 3) the radiometric soil reflectivity r_{radio} as derived from the L-band radiometer and the *in situ* measured temperature data.

To calculate r_{TDR} and r_{COUP}, we implemented a coherent radiative transfer model representing the soil as a stratified dielectric medium consisting of layers with uniform thickness d. The radiative model is based on a matrix formulation of the boundary conditions at the layer boundaries derived from Maxwell's equations [24]. The output of this algorithm is the soil reflectivity. The expected inputs are two soil profile vectors containing layer thickness and complex dielectric constants of the layer stack, wavelength, polarization, and observation angle α.

Due to the poor depth resolution of the measured *in situ* data (TDR water content and temperature measurements) and of the soil profiles from the COUP model, it was necessary to increase the resolution of these profiles to be used as input for the radiative transfer model. This was achieved by fitting third-order polynomials to the low-resolution profiles, from which soil profile vectors were constructed with a virtually increased depth resolution $d = 1$ mm.

As will be discussed later (Section IV-B), the radiometrically determined soil reflectivity r_{radio} for horizontal polarization is systematically smaller than the reflectivities r_{TDR} and r_{COUP}, which were calculated using the radiative transfer model. A better fit can be achieved if the radiative model is supplemented by an air-to-soil transition model considering dielectric mixing effects due to the small-scale surface structure [22] of the observed site. In a wider understanding, this model can also account for low plant canopy and thin snow layers on bare soil or for cavities and stones within the uppermost soil horizon.

Calculation of r_{TDR}: The dielectric profile vector required for calculating the reflectivity r_{TDR} was generated using the volumetric liquid water contents θ_{TDR} measured with the TDR probes and the temperatures T measured at the same depths (see Section II-A). For any θ_{TDR} the dielectric constant $\varepsilon_{\mathrm{TDR}}$ of the soil was deduced by applying the dielectric mixing model of Wang and Schmugge [25]. The depth-dependent soil properties used in the mixing model are the water content θ_0 at saturation ($=$ porosity) in cubic millimeters per cubic millimeter and clay content $s(z)$ and $c(z)$ in cubic kilograms per cubic kilogram, respectively

$$\begin{aligned} \theta_0(z) &= 0.45 - 2 \cdot 10^{-4}\, z \\ s(z) &= 0.40 - 1.8 \cdot 10^{-4}\, z \\ c(z) &= 0.278 + 2 \cdot 10^{-5}\, z. \end{aligned} \tag{11}$$

The above profiles were deduced by linear fitting to the soil properties listed in Table I.

The frequency and temperature dependence of the dielectric constant ε_{w} of pure free water used in the Wang and Schmugge model was calculated according to the model of Cole and Cole [26].

Calculation of r_{COUP}: The dielectric profile vector required for calculating r_{COUP} was generated from the soil water content profiles calculated with the numerical soil water and heat transport model COUP (see Section III-A). The COUP model yields profiles for the total volumetric water content θ_{tot} (frozen plus unfrozen water), volumetric liquid water content θ_l, and the soil temperature profiles T. To calculate the soil dielectric constant $\varepsilon_{\mathrm{COUP}}$ from these profiles, the semiempirical mixing model of Dobson [27] was applied. In addition to the three phases liquid water, air, and soil matrix [28], ice was considered in the mixing model as the fourth phase [29]

$$\begin{aligned} \varepsilon_{\mathrm{COUP}} = [&(\theta_0 - \theta_{\mathrm{tot}})\varepsilon_{\mathrm{air}}^{\eta} + \theta_l \cdot \varepsilon_{\mathrm{w}}^{\eta} \\ &+ (\theta_{\mathrm{tot}} - \theta_l)\varepsilon_{\mathrm{ice}}^{\eta} + (1 - \theta_0)\varepsilon_{\mathrm{matrix}}^{\eta}]^{1/\eta}. \end{aligned} \tag{12}$$

The dielectric constants of the air, ice, and soil matrix were assumed to be $\varepsilon_{\mathrm{air}} = 1$, $\varepsilon_{\mathrm{ice}} = 3.2 - \mathrm{j} \cdot 0.1$ and $\varepsilon_{\mathrm{matrix}} = 5.5 - \mathrm{j} \cdot 0.2$. The exponent η was set to 0.5, which is theoretically valid for an isotropic two-phase medium [30]. For the soil porosity θ_0, the profile given by (11) was chosen, and the dielectric constant ε_{w} of free water was calculated according to Cole and Cole [26].

Calculation of r_{radio}: The soil reflectivity r_{radio} was derived from the brightness temperature T_{B} measured with the radiometer pointing toward the area of observation. The reflectivity r_{radio} is related to the soil emissivity e by Kirchhoff's law [(8)], and e is derived from the soil temperature T_{A} and the brightness temperature T_{B} [(7)]. The soil temperature T_{A} was calculated according to (9), using the *in situ* measured temperature profile $T(z)$ with improved resolution as described above.

Air-to-Soil Transition Model: At the subwavelength scale, the dielectric transition between the footprint surface and the air does not appear as a sharp boundary. The surface incorporates irregularities (e.g., roughness, cavities, stones, low vegetation, and snow), which are laterally not resolved when observed at long wavelengths like L-band. This is accommodated by introducing a transition zone [22], wherein the proportion of soil matrix (bulk soil) is increasing with depth. The increasing portion of soil matrix is described by a function $F(z^*)$, which is mainly defined by the surface roughness. Therefore, $F(z^*)$ was derived from the normalized surface height distribution $G(z^*)$ by integrating over a so-called transition zone of thickness h (Fig. 2).

The dielectric properties of the transition zone are described by a two-phase isotropic dielectric mixing model [30] considering the depth-dependent fractions of the two phases air and bulk soil. This mixing approach describing the flattened transition from air to soil is nothing more than impedance matching between the dielectric constant of air and bulk soil. As illustrated in the left graph of Fig. 2, this yields a modified dielectric depth profile $\varepsilon_{\mathrm{struc}}$ (solid line) calculated from the original profile ε (dashed line) considering a structured transition zone.

The coordinate z^* in Fig. 2 is used as depth coordinate in the radiative transfer model for calculating the soil reflectivities r_{TDR} and r_{COUP}. As illustrated, z^* corresponds to the physical soil depth z shifted by $h/2$. For a Gaussian height distribution, the extension h can be related to the standard deviation σ of

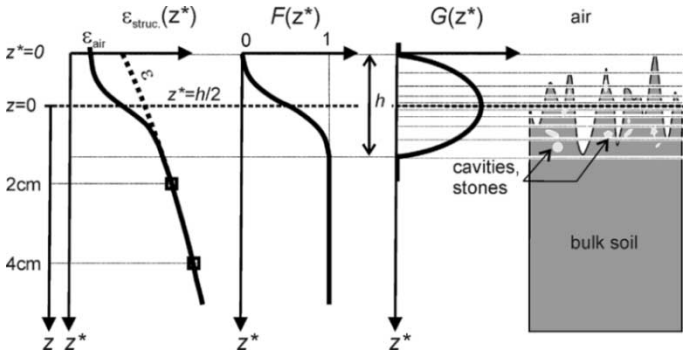

Fig. 2. Illustration of the impedance matching approach applied in the air-to-soil transition model. G = surface height distribution, F = transition function, $\varepsilon_{\mathrm{struc}}(\varepsilon)$ = dielectric profile considering (no) surface structure.

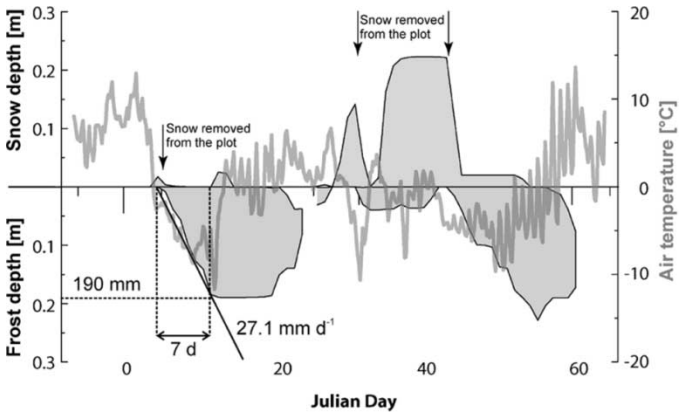

Fig. 3. Snow and soil frost depth on the experimental field plot simulated with the COUP model and air temperature measured at Zürich-Airport. The average frost front penetration velocity during the first spell of frost is estimated to be 27.1 mm/day.

the surface height, which corresponds to the measurable surface roughness within the footprint

$$\sigma \cong 0.25 \cdot h. \tag{13}$$

In general, σ has to be interpreted as the characteristic thickness of the near-surface layer in which the features roughness, cavities, stones, low vegetation, and snow occur. This interpretation makes σ a quantity that can be measured or estimated for the radiometrically observed site.

The small squares in the left graph of Fig. 2 indicate the local TDR measurements at the depths 2 and 4 cm. These depths are given relative to the depth $z = 0$ representing the average height of a laterally not resolved area of the order of $\lambda \times \lambda$ within the radiometer footprint.

It has been proven that the application of this model yields similar results to those of the roughness model based on physical optics [31]. However, the scope of application of the air-to-soil transition model is broader because it is not limited to pure surface roughness but can be applied to incorporate any dielectric inhomogeneities within a soil surface layer.

IV. Results

A. Soil Profile Simulations

Weather, Snow Cover, and Soil Frost Development: During the field experiment (December 2002 to March 2003 corresponding to Julian Day 14 to 62) two major frost events occurred at the Eschikon site (Fig. 3). On Julian Day 04, a ten-day period with no precipitation but continuously low air temperatures set in while the soil surface was more or less bare. The soil temperatures rapidly decreased, and soil frost penetrated to a depth of approximately 0.19 m within seven days corresponding to an average frost front penetration velocity of 27.1 mm/day. This cold period was followed by one week of air temperature fluctuating around the freezing point, with positive values during the day and negative during the night. During that period, daily melting and refreezing of the soil surface was observed, whereas the lower frost boundary hardly changed. At approximately Julian Day 23, the soil thawed, while the air temperature remained above 0 °C for almost one week. The second frost cycle was initiated with a short distinct drop of the air temperature around Julian Day 32. However, soil frost was not able to develop properly until we removed the snow from the plot on Julian Day 44. During this second phase, the frost layer reached again a maximum depth of about 0.20 m. After Julian Day 50, the air temperature started to rise, causing the soil to thaw until Julian Day 60.

Numerical Simulation of the Soil Water and Heat Conditions: The numerical model COUP was run for the time period of the field experiment. Hourly meteorological data from Zurich airport were used as driving input and the 4-m-deep simulated soil profile was divided into 15 layers of 0.04 m (close to the surface) to 1.0 m (at the base of the profile) thickness. Initially, the soil was in a rather wet state with a groundwater table at 0.4 m. The temperature in the uppermost meter of the profile was about 5 °C (Fig. 4). The simulated cooling of the soil after Julian Day 04 was in good agreement with the thermistor measurements.

Also, the decrease of the liquid soil water content in the uppermost soil layers due to freezing corresponded closely to the numerical model output albeit somewhat too rapidly compared with the TDR-measurements at 2 and 6 cm. This can partly be explained by the formulation and parameterization of the freezing characteristic curve in the model [(4)–(6)] and partly by the numerical scheme implying homogenous layers of a thickness smaller than the sphere of influence of the TDR probes. Volume-averaged TDR readings are, therefore, expected to respond more slowly to a sudden change of the liquid water content.

The daily freeze–thaw cycles at the soil surface between Julian Day 14 and 20 appeared distinctly in both model and measurements. Between the two frost periods, the TDR measurements showed somewhat more variation than the simulation, which we do not interpret as freezing phenomena, but snowmelt infiltration (not perfectly reproduced by the model). The simulation of the second soil frost penetration coincided again very well with the measurements, which also applies to the final thawing.

It can also be seen that below the frozen soil layer (25-cm depth), the simulated water content and temperature agreed well with the observed dynamics. Although the water content only marginally varied at this depth, reflecting the nearly saturated

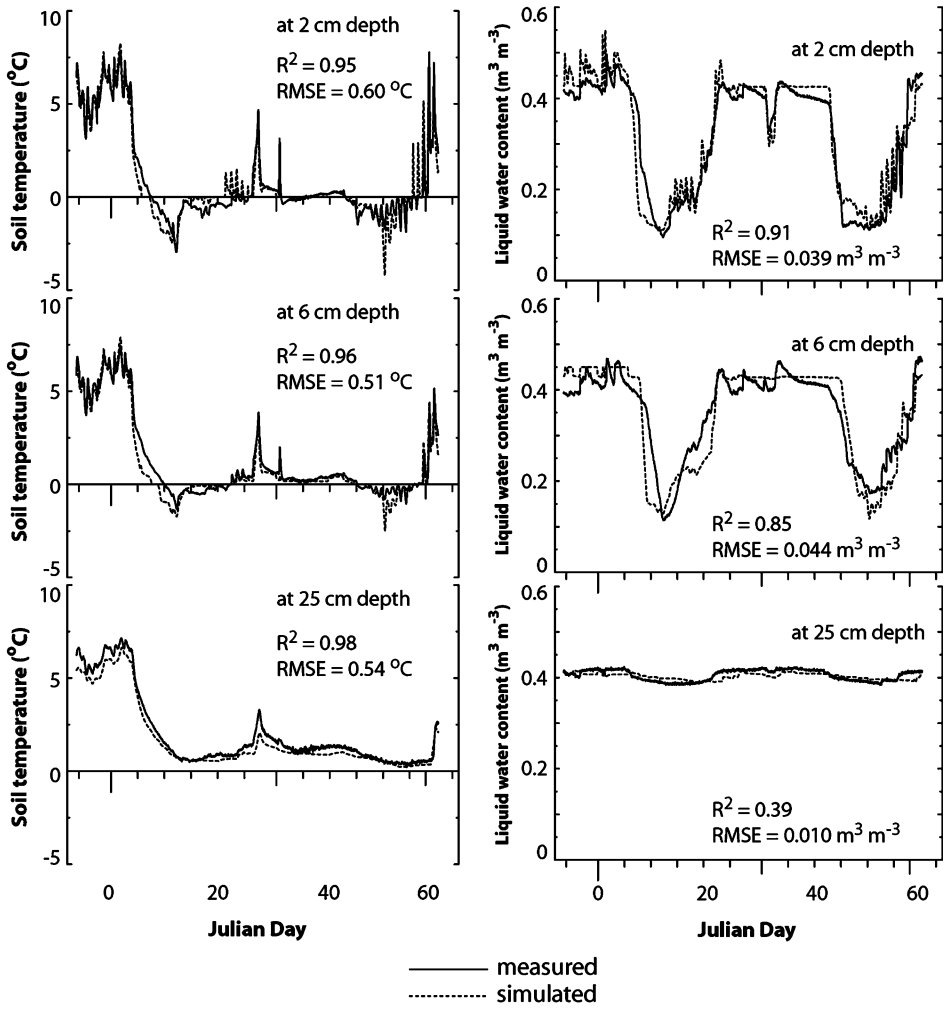

Fig. 4. Measured and simulated (left) temperature and (right) liquid water content for three different soil depths of the Eschikon field site over the time of the experiment.

conditions, the temperature decreased conspicuously toward the freezing point.

Overall, the correspondence between the *in situ* measurement and the simulated prediction was excellent, which justifies using the simulated soil moisture profiles for calculating microwave soil reflectivity (see Section IV-B).

B. Comparison of Soil Reflectivities

The soil reflectivity is used to compare the radiometric measurements with *in situ* measurements and simulated soil data. Fig. 5 shows the three corresponding soil reflectivities r_{TDR}, r_{COUP}, and r_{radio} for horizontal polarization (see Section III-C). The data are plotted for the whole measurement period.

As can be seen, the three soil reflectivities closely follow the climatic pattern, including the two frost spells (compare Section IV-A).

The penetration of the freezing front reduces the free liquid water to extremely low values. Due to the lower dielectric constant of ice, this results in a pronounced decrease of the dielectric constant of the upper soil region. This results in the observed reduction in soil reflectivity, when the soil starts to freeze.

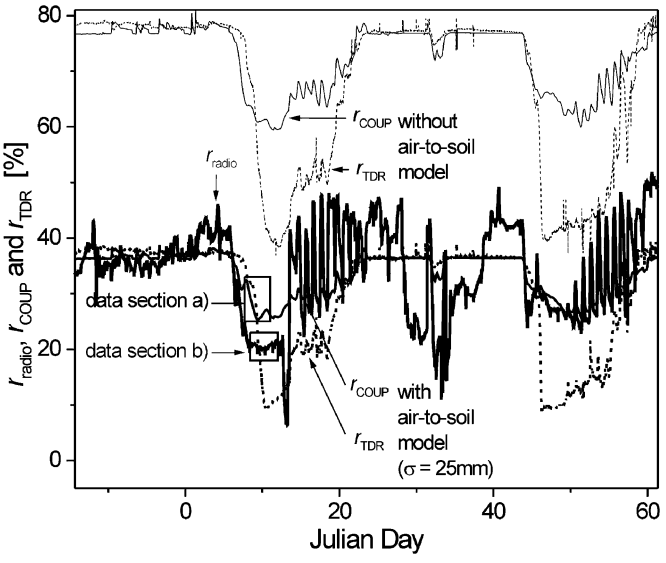

Fig. 5. Comparison between soil reflectivities r_{radio}, r_{COUP}, and r_{TDR} for horizontal polarization and $\alpha = 70°$ over the measurement period from December 17, 2002 to March 2, 2003. The data sections a) and b) within the two windows will be used in Section IV-C and Fig. 6(a) and (b) to estimate the frost front penetration velocity.

Qualitatively spoken, the reflectivities r_{TDR} and r_{COUP} calculated without considering the air-to-soil transition model are in good agreement for wet periods (thin dashed and solid lines). When the topsoil is frozen, the observed reduction in the r_{TDR} data is more pronounced than the reduction in the r_{COUP} data. This difference in the dynamics of the data can be explained by the following considerations. As a consequence of the reduction of the liquid water content within the topsoil, the cylindrically shaped measurement volumes of the TDR probes are extended in their radial direction. Therefore, the measurement volume of the uppermost probe may even include air from above the soil surface. This results in a systematic underestimation of the topsoil dielectric constant (and water content) at frozen (dry) conditions. Since the soil reflectivity r_{TDR} is mostly affected by the topsoil dielectric constant, it is systematically underestimated at frozen (dry) conditions.

The radiometrically determined reflectivity r_{radio} (bold gray line) is systematically lower than r_{TDR} and r_{COUP} (thin dashed and solid lines) calculated without considering the air-to-soil transition model. This deviation can be diminished by considering structural features occurring within a superficial layer of the site by applying the air-to-soil transition model described in Section III-C. In this model extension, the transition between the footprint surface and the air is described as a gradual transition (impedance matching approach) from air to bulk soil. Aside from soil surface roughness, this approach may also account for low plant canopy, thin snow layers, or for cavities and stones within the near-surface layer. The characteristic thickness σ of this surface layer in which these features occur was obtained by an arbitrary guess to be $\sigma = 25$ mm. However, this estimation was compatible with the visual inspection of the footprint surface. The resulting reduction of the dielectric gradient at the surface (compare left graph of Fig. 2) yields a reduction of the calculated reflectivities and thus a better agreement with the radiometric soil reflectivity r_{radio} (see bold dotted and solid lines in Fig. 5).

The daily fluctuations in the radiometrically determined soil reflectivity r_{radio} during the two thawing periods (Julian Day 15–22 and 50–60) are much more pronounced compared to the soil reflectivities r_{TDR} and r_{COUP}. This could be explained by the daily occurrence of a thin liquid water layer at the very top of the soil, affecting the radiometric soil reflectivities r_{radio} more distinctly.

Just after Julian day 13, a short-time drop in the air temperature and the simultaneous occurrence of a snow layer (Fig. 3) might be the reason for the observed drop in r_{radio} depicted in Fig. 5.

The radiometric reflectivities included daily occurring sharp drops, which were identified to be caused by solar radiation reflected by the site surface and transmitted to the radiometer facing toward the sunset. These spikes were eliminated from the data to enable the following discussion of coherent effects.

C. Estimation of Frost Front Penetration Velocity

The penetration velocity of the frost front is estimated by analyzing the temporal oscillating behavior of soil reflectivities as observed during the frost front penetration. We hypothesized that the oscillating behavior of the soil reflectivities is associated

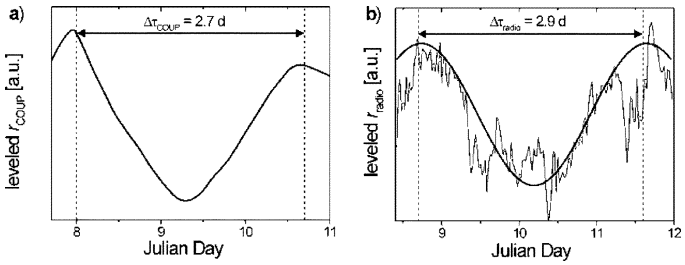

Fig. 6. Leveled reflectivities r_{COUP} and r_{radio} during penetrating frost front taken from Fig. 5 [data sections a) and b)]. The oscillating behavior is interpreted to be due to coherent effects.

to the coherent superposition of partially reflected electromagnetic fields within the soil profile.

In the following investigation, the modeled and the radiometric measured soil reflectivity data r_{COUP} and r_{radio} from Fig. 5 are considered. These data are restricted to the data sections a) and b) during the first frost spell. The second frost spell was not analyzed for the following reasons: 1) during the second frost spell the footprint area was covered with a snow layer; 2) the temperatures and their daily fluctuations were more pronounced compared to the first spell of frost resulting in partial surface thawing. This may result in a layer of liquid water at the surface of the footprint that attenuates radiation from deeper soil layers.

Therefore, the observation of a coherent behavior related to the frost front depth is very unlikely. Based on the data sections a) and b) of the soil reflectivities r_{COUP} and r_{radio}, the corresponding frost penetration velocities v_{COUP} and v_{radio} are calculated as

$$v_{\mathrm{COUP}} = \frac{\Delta z_{\mathrm{f}}}{\Delta\tau_{\mathrm{COUP}}} \quad v_{\mathrm{radio}} = \frac{\Delta z_{\mathrm{f}}}{\Delta\tau_{\mathrm{radio}}}. \tag{14}$$

r_{COUP} and r_{radio} are the elapsed time intervals between the first two consecutive maxima of the soil reflectivity data r_{COUP} and r_{radio} during the first soil freezing event. The spatial quantity Δz_{f} is the advancement of the frost depth yielding to the first two consecutive maxima of the soil reflectivity. In the following, the extraction of the time intervals $\Delta\tau_{\mathrm{COUP}}$ and $\Delta\tau_{\mathrm{radio}}$ from the reflectivity data and the calculation of the spatial quantity Δz_{f} is described.

Time Intervals $\Delta\tau_{\mathrm{COUP}}$ and $\Delta\tau_{\mathrm{radio}}$: In order to determine the elapsed time intervals $\Delta\tau_{\mathrm{COUP}}$ and $\Delta\tau_{\mathrm{radio}}$, fitted baselines were subtracted from the data sections a) and b) of the soil reflectivity data r_{COUP} and r_{radio} yielding to the leveled data sequences depicted in Fig. 6(a) and (b). After manually suppressing the daily occurring sharp peaks in r_{radio}, the data sequences exhibit a temporal oscillation with similar periodicities. The elapsed time intervals between the first two consecutive maxima are $\Delta\tau_{\mathrm{COUP}} = 2.7$ days for the r_{COUP} data and $\Delta\tau_{\mathrm{radio}} = 2.9$ days for the r_{radio} data.

Calculation of ΔZ_{f}: To investigate the coherent behavior of the soil reflectivity as expected during downward freezing soil, we calculated soil reflectivities for a set of hypothetical (not physically based) dielectric profiles $\varepsilon(z)$ imitating a frost front penetration. The dielectric profiles were parameterized with two dielectric levels ε_{f} and $\varepsilon_{\mathrm{uf}}$ representing the frozen and unfrozen

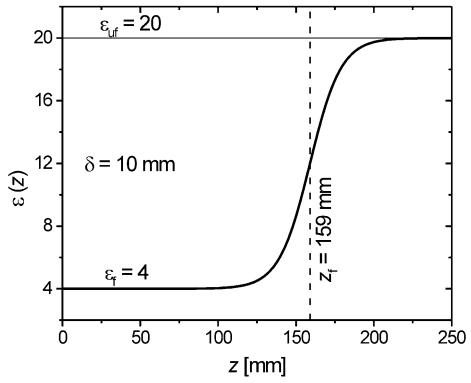

Fig. 7. Hypothetical dielectric profile $\varepsilon(z)$ imitating a frost front located at the depth $z_{\rm f}$.

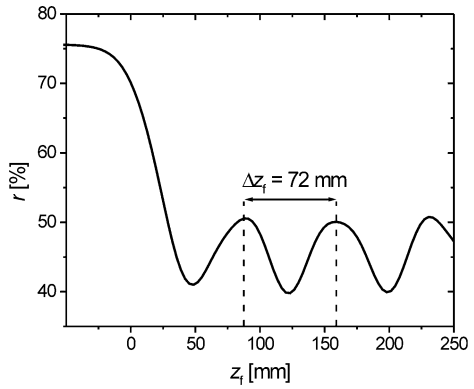

Fig. 8. Reflectivity r for horizontal polarization and $\alpha = 70^\circ$ calculated for a set of hypothetical dielectric profiles $\varepsilon(z)$ as a function of the frost front depth parameter $z_{\rm f}$.

soil state, the depth $z_{\rm f}$ of the transition between frozen and unfrozen state, and the steepness parameter δ describing the width of the transition zone

$$\varepsilon(z) = \varepsilon_{\rm f} + (\varepsilon_{\rm uf} - \varepsilon_{\rm f}) \cdot \left[1 - \frac{1}{\exp\left(\frac{z - z_{\rm f}}{\delta}\right) + 1}\right]. \qquad (15)$$

The term in the squared brackets is the Fermi-distribution centered at the $z_{\rm f}$ with steepness δ. Fig. 7 shows a plot of the profile given by (15) with $z_{\rm f} = 159$ mm, $\delta = 10$ mm and the dielectric constants $\varepsilon_{\rm f} = 4$ and $\varepsilon_{\rm uf} = 20$, which are reasonable values for wet frozen and unfrozen soils [32].

From a set of dielectric profiles $\varepsilon(z)$ with variable $z_{\rm f}$, we calculated L-band reflectivities at the observation angle $\alpha = 70^\circ$ for horizontal polarization using the coherent radiative transfer model described in Section III-C. Fig. 8 shows the dependence of the reflectivity from the frost depth parameter $z_{\rm f}$. The first two consecutive local maxima occur at $z_{\rm f} = 80$ mm and $z_{\rm f} = 159$ mm. This corresponds to an advancement of the frost front depth from the first to the second maximum of $\Delta z_{\rm f} = 72$ mm.

Further calculations showed that the dielectric constant $\varepsilon_{\rm f}$ of the frozen soil is the dominant parameter affecting $\Delta z_{\rm f}$ of the frost depth propagation. The parameters δ and $\varepsilon_{\rm uf}$ as well as an imaginary part of $\varepsilon_{\rm f}$ affect the amplitude of the oscillating behavior of the reflectivity, but play only a subsidiary role for the spatial periodicity $\Delta z_{\rm f}$. For example, the variation of the less sensitive parameter $15 \leq \varepsilon_{\rm uf} \leq 30$ with $\varepsilon_{\rm f} = 4$ and $\delta = 10$ mm yields to the narrow range of 73 mm $\leq \Delta z_{\rm f} \leq$ 70 mm. The variation of the sensitive parameter $\varepsilon_{\rm f}$ with $\varepsilon_{\rm uf} = 20$ and $\delta =$ 10 mm within a reasonable range of $3.5 \leq \varepsilon_{\rm f} \leq 4.5$ for the dielectric constant of the frozen soil covers the wider range of 68 mm $\leq \Delta z_{\rm f} \leq$ 77 mm.

Assuming that the temporal periods $\Delta\tau_{\rm COUP}$ and $\Delta\tau_{\rm radio}$ and the spatial period $\Delta z_{\rm f}$ are assigned to the same advancement of the frost front enables calculation of the frost penetration velocities $v_{\rm COUP}$ and $v_{\rm radio}$ according to (14)

$$v_{\rm COUP} \approx 27 \text{ mm/day} \quad v_{\rm radio} \approx 25 \text{ mm/day}. \qquad (16)$$

From the COUP simulations of the frost depths during the first freezing period, the frost penetration velocity was estimated to be 27.1 mm/day (Fig. 3) by linear approximation to the advancing frost front. This is in good agreement with the penetration velocities $v_{\rm COUP}$ and $v_{\rm radio}$ calculated above.

It should be mentioned that the $r_{\rm TDR}$ data during the penetrating frost front showed no coherent behavior. It is supposed that this is due to the deterioration of the depth resolution of the TDR water content profiles because of the increase of the TDR measurement volume. This leads to an overestimation of the TDR measured liquid water content within the frozen soil part, which reduces the dielectric gradient to the unfrozen soil, hindering the occurrence of coherent effects.

V. Conclusion

The L-band radiometer measurements obtained during a winter period at a field site clearly revealed the high sensitivity of microwave emission to ground surface freezing.

We demonstrated that the quantitative consistency between the radiometrically observed reflectivity and the reflectivities based on *in situ* measured and modeled profiles was significantly improved by applying an impedance matching approach. With this approach, we took structural effects into account such as soil surface roughness, low plant canopy, thin snow layers, cavities, and stones showing up within a near-surface layer of characteristic thickness σ. With $\sigma = 25$ mm, we obtained the best agreement between the soil reflectivities. The value for σ was obtained through an arbitrary guess, which is consistent with the visual inspection of the footprint surface.

The potential of estimating the soil frost penetration velocity from the radiometrically measured L-band radiation was demonstrated by means of evaluating the observed coherent behavior of the soil reflectivity during an advancing frost front. The time period between the first two maxima of the observed oscillation was determined to be 2.9 days. The calculated soil reflectivities based on the hypothetical dielectric profiles imitating a superficial frozen soil revealed an advancement of the frost front of 72 mm to generate the first two consecutive maxima. From this, we estimated the radiometrically observed penetration velocity of the frost front to be 25 mm/day. This was in good agreement with the frost penetration velocity estimated with the numerical soil water and heat model.

ACKNOWLEDGMENT

The authors are grateful to C. Stamm for the initiation of the presented experiment. Special thanks to K. Schneeberger who contributed to this work with her extensive experience in radiometric remote sensing of soil moisture.

REFERENCES

[1] L. Oygarden, "Rill and gully development during an extreme winter runoff event in Norway," *CATENA*, vol. 50, no. 2–4, pp. 217–242, 2003.
[2] Y. Kerr, P. Waldteufel, J.-P. Wigneron, J.-M. Martinuzzi, J. Front, and M. Berger, "Soil moisture retrieval from space: The soil Moisture and Ocean Salinity (SMOS) mission," *IEEE Trans. Geosci. Remote Sensing*, vol. 39, pp. 1729–1735, Aug. 2001.
[3] P.-E. Mellander, K. Bishop, and T. Lundmark, "The influence of soil temperature on transpiration: A plot scale manipulation in a young Scots pine stand," *Forest Ecol. Manage.*, to be published.
[4] M. Phillips, S. M. Springman, and L. U. Arenson, *Permafrost—Proc. 8th Int. Conf. Permafrost*, vol. 1380, Zurich, Switzerland, July 21–25, 2003, p. 2003.
[5] E. Njoku and J.-A. Kong, "Theory for passive microwave remote sensing of near-surface soil moisture," *J. Geophys. Res.*, vol. 82, pp. 3108–3118, 1977.
[6] T. Jackson and T. Schmugge, "Passive microwave remote sensing system for soil moisture: Some supporting research," *IEEE Trans. Geosci. Remote Sensing*, vol. 27, pp. 225–235, Mar. 1989.
[7] T. Zhang and R. L. Armstrong, "Soil freeze/thaw cycles over snow-free land detected by passive microwave remote sensing," *Geophys. Res. Lett.*, vol. 28, no. 5, pp. 763–766, 2001.
[8] T. J. Schmugge and T. J. Jackson, "Observation of coherent emissions from soils," *Radio Sci.*, vol. 33, no. 2, pp. 267–272, 1998.
[9] C. Mätzler, D. Weber, M. Wüthrich, K. Schneeberger, C. Stamm, H. Wydler, and H. Flühler, "ELBARA, the ETH L-band radiometer for soil-moisture research," in *Procs. IGARSS*, Toulouse, France, July 2003.
[10] K. Schneeberger, C. Stamm, C. Mätzler, and H. Flühler, "Estimating soil hydraulic properties from time-series of L-band measured water contents," in *Procs. IGARSS*, Toulouse, July 21–25, 2003.
[11] A. Fehlmann, "Preliminary experiments in Eschikon to determine soil properties," Inst. Terrestrial Ecol., ETH Zürich, Zürich, Switzerland, Int. Rep., 2001.
[12] K. Schneeberger, C. Stamm, C. Mätzler, and H. Flühler, "Ground-based dual-frequency radiometry of bare soil at high temporal resolution," *IEEE Trans. Geosci. Remote Sensing*, vol. 42, pp. 588–595, Mar. 2004.
[13] P.-E. Jansson and D. Moon, "A coupled model of water, heat and mass transfer using object orientation to improve flexibility and functionality," *Environ. Model. Software*, vol. 16, no. 1, pp. 37–46, 2001.
[14] M. Stähli, P.-E. Jansson, and L.-C. Lundin, "Soil moisture redistribution and infiltration in frozen sandy soils," *Water Resources Res.*, vol. 35, pp. 95–103, 1999.
[15] D. Stadler, H. Flühler, and P.-E. Jansson, "Modeling vertical and lateral water flow in frozen and sloped forest soil plots," *Cold Reg. Sci. Technol.*, vol. 26, no. 3, pp. 181–194, 1997.
[16] D. Gustafsson, M. Stähli, and P.-E. Jansson, "The surface energy balance of a snow cover: Two different simulation models and measurements," *Theoret. Appl. Climat.*, vol. 70, no. 1–4, pp. 81–96, 2001.
[17] L. A. Richards, "Capillary conduction of liquids in porous mediums," *Physics*, vol. 1, pp. 318–333, 1931.
[18] M. T. Van Genuchten, "A closed form equation for predicting the hydraulic conductivity of unsaturated soils," *Soil Sci. Soc. Amer. J.*, vol. 44, pp. 892–898, 1980.
[19] P.-E. Jansson and L. Karlberg, "Coupled heat and mass transfer model for soil-plant-atmosphere systems," Div. Land and Water Resources, Royal Inst. Technol., Stockholm, Sweden, ISSN 1400–1306, 2001.
[20] F. Ulaby, R. Moore, and A. Fung, *Microwave Remote Sensing Active and Passive. Microwave Remote Sensing and Fundamentals and Radiometry*. Reading, MA: Addison-Wesley, 1981, vol. I.
[21] T. Schmugge, "Remote sensing of soil moisture," in *Hydrological Forecasting*, M. Anderson and T. Burt, Eds. New York: Wiley, 1985, pp. 101–124.
[22] K. Schneeberger, M. Schwank, C. Stamm, P. de Rosnay, C. Mätzler, and H. Flühler, "Topsoil properties influencing soil moisture retrieval by microwave radiometry," Water Resources Res., to be published.
[23] F. Ulaby, R. Moore, and A. Fung, *Microwave Remote Sensing Active and Passive*. Norwood, MA: Artech House, 1986, vol. III, From Theory to Applications.
[24] *Handbook of Optics*, vol. 1, M. Bass, E.W. Van Stryland, R. Williams, and W. L. Wolfe, Eds., McGraw-Hill, New York, 1995, pp. 42.9–42.14.
[25] J. Wang and T. Schmugge, "An empirical model for complex dielectric permittivity of soils as a function of water content," *IEEE Trans. Geosci. Remote Sensing*, vol. GE-18, pp. 288–295, 1980.
[26] K. S. Cole and R. H. Cole, "Dispersion and absorption in dielectrics," *J. Chem. Phys.*, vol. 9, pp. 341–351, 1941.
[27] M. C. Dobson, F. T. Ulaby, M. T. Hallikainen, and M. A. El-Rayes, "Microwave dielectric behavior of wet soil, II: Dielectric mixing models," *IEEE Trans. Geosci. Remote Sensing*, vol. GE-23, pp. 35–46, Jan. 1985.
[28] K. Roth, R. Schulin, H. Flühler, and W. Attinger, "Calibration of time domain reflectometry for water content measurement using a composite dielectric approach," *Water Resources Res.*, vol. 26, no. 10, pp. 2267–2273, 1990.
[29] M. Stähli and D. Stadler, "Measurement of water and solute dynamics in freezing soil columns with time domain reflectometry," *J. Hydrol.*, vol. 195, pp. 352–369, 1997.
[30] J. R. Birchak, C. G. Gardner, J. E. Hipp, and J. M. Victor, "High dielectric constant microwave probes for sensing soil moisture," *Proc. IEEE*, vol. 62, pp. 93–98, 1974.
[31] F. Ulaby, R. Moore, and A. Fung, *Microwave Remote Sensing Active and Passive*. Reading, MA: Addison-Wesley, 1981, vol. II, Microwave Remote Sensing and Fundamentals and Radiometry, p. 1009.
[32] C. Mätzler, "Passive microwave signature catalog 1989 –1992 (vol. 1)," Univ. Bern, Bern, Switzerland, IAP-Rep., 1993.

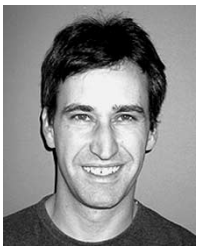

Mike Schwank received the Ph.D. degree in physics from the Swiss Federal Institute of Technology Zürich (ETH), Zürich, Switzerland, in 1999. The topic of his Ph.D. dissertation was "nano-lithography using a high-pressure scanning-tunneling microscope."

From 2000 to 2002, he was a Research and Development Engineer in the field of micro-optics. He is currently a Senior Research Assistant with the Institute of Terrestrial Ecology, ETH-Zürich. His research involves practical and theoretical aspects of radiometry applied to soil moisture detection

Manfred Stähli received the Ph.D. degree in environmental physics from the Swedish University of Agricultural Sciences, Uppsala, Sweden, in 1998. His research focused on heat and water transport processes in seasonally frozen soils.

In 1998, he became a Postdoc with the Institute of Terrestrial Ecology, Swiss Federal Institute of Technology Zürich, Zürich, Switzerland, and since 2001, he has been working with the Swiss Federal Research Institute WSL in the Forest Hydrology Team. He is currently studying snow hydrological issues, some of them related to frozen soil conditions.

Hannes Wydler is an Electrical Engineering Technician. Since 1983, he has been supporting the Soil Physics Group of the Institute of Terrestrial Ecology, Swiss Federal Institute of Technology Zürich, Zürich, Switzerland, in developing experimental setups.

Joerg Leuenberger is a skilled Forester and has been a member of the technical staff of the Institute of Terrestrial Ecology (Soil Physics), ETH Zürich, Zürich, Switzerland, since 1971. His main working tasks are to support the group in designing field experimental setups. He is currently involved in planning the experimental setup for ongoing radiometric experiments.

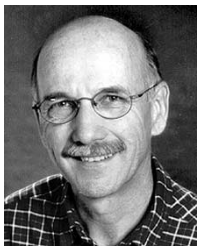

Christian Mätzler (M'96–SM'03) studied physics at the University of Bern, Bern, Switzerland, with subsidiaries in mathematics and geography.

After his doctoral thesis (1974) in solar radio astronomy, he made Postdoctoral Studies at the NASA Goddard Space Flight Center, Greenbelt, MD, and at the Swiss Federal Institute of Technology Zürich, Zürich, Switzerland. He is currently Titularprofessor in applied physics and remote sensing, leading the Project Group on Radiometry for Environmental Monitoring, Institute of Applied Physics, University of Bern. His experimental studies have concentrated on surface-based microwave (1–100 GHz) signatures for active and passive microwave remote sensing of snow, ice, soil, vegetation, and atmosphere, including precipitation, clouds, and the boundary layer, and on the development of methods for dielectric measurements of these media, with complementary work at optical wavelengths. He is interested in meteorological applications of remote sensing and in improvements of the physical understanding of the processes involved. Based on the experimental work of his group, he has developed and tested microwave (1–100 GHz) propagation, transmission, emission, scattering, and dielectric models of snowpacks and of the atmosphere.

Dr. Mätzler is a member of the International Glaciological Society.

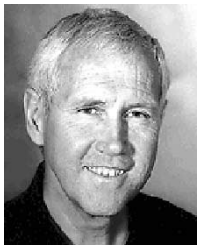

H. Flühler studied at the Department of Forest Sciences, Swiss Federal Institute of Technology (ETH) Zürich, Zürich, Switzerland, and received the Ph.D. degree in 1972. He did his postgraduate studies in soil physics at the ETH Zürich, in 1973, and at the University of California, Riverside, from 1974 to 1976.

From 1977 to 1980, he led the Biophysics Group at the Federal Institute for Forestry Research, and from 1980 to 1983, he chaired the Vegetation and Soil Section at this institute. Since 1983, he has been a Professor of soil physics at ETH Zürich. His research is focused on transport processes in soil, specifically in methodology, but also in relation to environmental applications.